Lithuanian Journal of Physics
Vol. **63**, No. 3, pp. 173–190 (2023)

ISSN 1648-8504 eISSN 2424-3647
DOI: https://doi.org/10.3952/physics.2023.63.3.8

INVESTIGATION OF BLUR KERNEL OF TERAHERTZ IMAGES

V. Abramova [a, b], S. Abramov [a], V. Lukin [a], I. Grigelionis [b],

L. Minkevičius [b], and G. Valušis [b]

[a] *Department of Information-Communication Technologies, National Aerospace University,*
Chkalova 17, 61070 Kharkiv, Ukraine
[b] *Department of Optoelectronics, Center for Physical Sciences and Technology, Saulėtekio 3, 10257 Vilnius, Lithuania*
Email: viktoriia.abramova@ftmc.lt

Received 5 October 2023; accepted 6 October 2023

The paper discusses issues of digital processing of terahertz images. It is shown that despite the improvement of the hardware part of imaging setups, the acquired images still often have a low resolution and suffer from noise and blurring effects. Thus, to improve their visual quality, it is advisable to use special digital processing methods. While some progress has already been made in terms of denoising of terahertz images, the research of their deblurring is only at the very early stage. Therefore, this paper attempts to analyze the properties of blur functions for real terahertz images to further use them while designing a corresponding deblurring technique. For this purpose, the phase-only image method has been used. A study of blur properties for the three most common blur types (defocus, motion and Gaussian blur) has shown that for test images they can be distinguished and their main parameters can be assessed. However, the application of this method to real terahertz images has shown that the blur characteristics in them are very different from the ones obtained for modelled examples. The real blur demonstrates a quite complex behaviour and estimating its kernel requires additional research.

Keywords: terahertz imaging, image deblurring, blur kernel estimation

1. Introduction

Recent developments in terahertz (THz) imaging aim towards applications in a wide variety of fields extending from security and medicine to ancient art inspection [1–11]. However, one has to deal with the trade-off between the ease of use, cost and compactness of THz imaging setups, and the quality of the obtained images. On the one hand, operation at higher frequencies allows one to obtain images with higher detail, yet on the other hand, the equipment for the upper THz frequency range is complex and not cost-efficient. At the same time, low frequency commercial THz sources are more compact, user-friendly and have a higher optical output power while suffering from a low spatial resolution, which results in deterioration in the quality and information value of the obtained images.

It should be noted that image quality greatly depends on the imaging method used. In the simplest case – direct THz imaging – only the power of terahertz radiation transmitting through or reflecting from the object under study is recorded, leading to the loss of information on small details, which is especially true if the object is low-absorbing. More advanced and promising are homodyne [2] and heterodyne [3] techniques that allow one to also record phase information. Yet, they require a more elaborate equipment and are more sensitive to optical alignment, so their use outside scientific laboratories is still challenging.

One more limiting factor of THz imaging is the low speed of image acquisition in the commonly used raster scan technique. Since in this method the image is acquired pixel-by-pixel, obtaining images with a high resolution turns out to be a very time-consuming task. Thus, the resolution of THz images is often quite low [5, 16].

Finally, the quality of terahertz images significantly depends on the shooting conditions, the material of the object under study, and equipment parameters [1], which due to long acquisition time are not easy to stabilize. Because of this, the resulting images are often highly blurred and noisy, making it very difficult to extract useful information even if the spatial resolution is acceptable.

Most of the mentioned problems are difficult to solve at a technical level, so the use of digital processing methods seems promising. Despite the obvious potential, digital processing of THz images is only at the very beginning of its development, limited mainly to object and edge detection [4]. As for operations aimed at improving quality, there are only a few attempts to increase the resolution of THz images using neural networks [5, 16], as well as the use of neural networks for detection of highly blurred images that are supposed to be excluded from further consideration [7].

However, taking into account the complexity of the THz image acquisition process, leaving out poor quality images is not always a good option and trying to enhance them can be a reasonable choice. In one of our recent papers [8], it has been shown that, with some adjustments, the methods initially designed for optical and radar images [9–22] can be successfully applied to THz images as well. The denoising method proposed in [8] allowed one to remove most of the visible noise from the considered THz images thus making them more convenient for further visual inspection, yet the problem of their blurring was not solved and even became more acute. This article aims to continue the research in this area and to investigate the characteristics of blur in THz images acquired at a frequency of 0.1 THz by means of a relatively compact imaging setup. The obtained information is supposed to be further used while designing a corresponding deblurring method.

2. Challenges of image deblurring

Generally, a blurred image I_b can be presented as follows:

$$I_b = \Phi(I_s, \theta_b). \tag{1}$$

Here I_s is the latent sharp version of the blurred image I_b, Φ is the image blur function, and θ_b is the parameter vector [23]. Here, both I_s and I_b are matrices, where distances from the origin in the horizontal and vertical directions are described by coordinates x and y, respectively, yet they are omitted for the convenience of perception.

Commonly, blurred images are modelled as a convolution of the latent sharp image with the blur kernel

$$I_b = I_s \otimes k, \tag{2}$$

where k is the blur kernel that differs depending on the blur type and its parameters and $\otimes$ denotes the convolution operation. The most common types are defocus (out-of-focus) blur, motion blur and Gaussian blur [23–25].

The defocus blur appears if the captured scene is not in the focus plane of the sensor but at some distance from it. This kind of blur may affect the whole image or just some parts of it if those appear to be outside the focus plane while the rest of the scene is close to it. The kernel of defocus blur is usually modelled as follows:

$$k(x,y) = \begin{cases} \dfrac{1}{\pi r^2}, \text{ if } (x-x_0)^2 + (y-y_0)^2 \le r^2, \\ 0. \end{cases} \tag{3}$$

Here (x_0, y_0) is the centre of blur kernel and r is the radius of blur [25].

The motion blur appears if there is the relative motion of the sensor or the object in the scene that is faster than the sensor exposure time. Visually the motion blur pronounces as streaking or smearing of image pixels in a certain direction. Apart from moving objects, camera shake or too long exposure time may become the reasons for the motion blur [23, 26, 27]. In simple cases, the motion blur can be modelled using shift-invariant kernels; for instance, it can be characterized by blur length and shifting angle [26]. However, more complicated cases of the motion blur require complex models that are often difficult to formalize [27–30].

Gaussian blur is the result of convolving an image with the 2D Gaussian kernel

$$k(x,y) = \frac{1}{2\pi\sigma^2} \mathrm{e}^{-\frac{x^2+y^2}{2\sigma^2}}, \tag{4}$$

where σ is the standard deviation of the Gaussian distribution. In Eq. (4), the function peak is located at (0, 0). Alternatively, the 2D Gaussian surface can be given in a general form as

$$k(x,y) = A\mathrm{e}^{-\left(a(x-x_0)^2+2b(x-x_0)(y-y_0)+c(y-y_0)^2\right)}, \quad (5)$$

where A is the centre peak height, x_0, y_0 are its coordinates, and a, b, c are the shape and angle regulating coefficients [25]. Unlike the other types of blur, the Gaussian blur usually appears in an image not at the stage of image capturing, but as a result of its further processing. It is widely used in graphics software to reduce image noise or detail, for example, as pre-processing before image downscaling. The Gaussian blur is a low-pass filter, attenuating high-frequency components of the image [31]. Therefore, if an image has been subjected to processing that affects high spatial frequencies, this may result in its blurring, which, under certain conditions, may resemble the Gaussian blur in appearance and behaviour.

In real-world situations, multiple factors can contribute to blur simultaneously, which creates the so-called mixed blur. The typical example of the mixed blur is a combination of motion and defocus blurs that appears if a fast-moving object is captured at an out-of-focus distance [23].

The goal of image deblurring is to recover a sharp latent image, which is usually achieved by finding the inverse of the blur function as

$$I_{\mathrm{db}} = \Phi^{-1}(I_{\mathrm{b}}, \theta_{\mathrm{b}}), \quad (6)$$

where I_{db} is the deblurred image (an estimate of the sharp image) and Φ^{-1} is the deblurring model. If the blur kernel is given, the problem is also known as non-blind deblurring. To reconstruct sharp images, non-blind deblurring methods use natural image priors [32, 33] to provide image deconvolution either in the spatial [34] or in the frequency [35, 36] domain. However, even if the true blur kernel is available, the task is still challenging because, apart from a significant loss of high frequency information, images also contain sensor noise that becomes visible after restoration. Moreover, there are often defects like ringing edges, artifacts and oversaturated regions in the deblurred images [37, 38].

In blind deblurring, both the latent image and the blur kernel are unknown, so they should be estimated from a given blurry image. The problem, however, is highly ambiguous, since multiple pairs of I_{s} and k can produce the same blurry image I_{b} [39]. Therefore, it is common to formulate the task of blind deblurring within a MAP framework [40] with priors on blur kernels or latent images, which means that specific methods are designed for certain types of blur and images with lots of additional restrictions [23, 41]. Advances in deep learning have brought image deblurring to a new level, introducing blind methods able to provide reasonable performance for various scenarios [23, 42, 43]. Yet, the problem of generalization was not solved and even became more acute, since the success of these methods greatly depends on the consistency between the training and testing datasets.

Thus, in order to select the approach that has the highest adaptation potential for deblurring of terahertz images, we need to obtain some prior information. This can be done by studying the image acquisition process in order to identify possible sources of blur, as well as by examining the obtained images using special image processing tools [26, 39, 41].

3. Experiment setup and the obtained dataset of terahertz images

The research object of our experiment was a sample cut out of a car tire with a thread mimicking a dielectric material with a rich surface topology. The average depth of the thread reached about 6 mm. The sample was mounted on a metallic frame with a 50 × 50 mm opening as demonstrated in Fig. 1. Also, a metal bushing serving as a reference was added on the holder at the plane of the top tire surface. The imaging experiment was performed in the reflection mode in the free space, according to the scheme depicted in Fig. 1. Here, the Gunn diode equipped with a horn antenna and emitting ~30 mW power at 100 GHz with electric field orientation along the y axis was used as a radiation source. It was electronically modulated at a frequency of 1 kHz. The output radiation was collimated using a high numerical aperture off-axis parabolic mirror (OAP2) and divided by a 50:50 silicon beamsplitter (BS). One of the collimated beams was focused onto the sample at the right angle by another off-axis parabolic mirror (OAP1). The reflected beam was collimated by the same OAP1 mirror and reached BS which split it once again, directing its part to a plasmonic field-effect transistor (FET) THz sensor through an OAP3 mirror. The scanning along

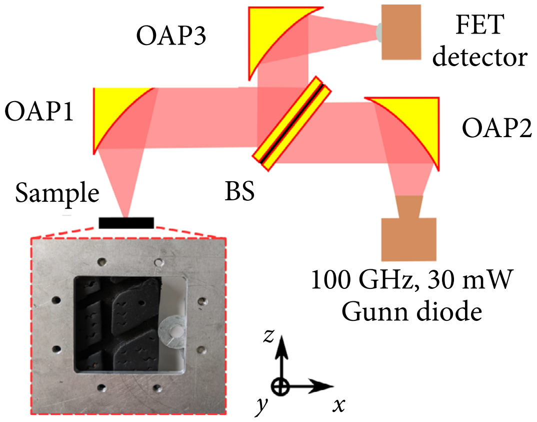

Fig. 1. The photo of the car tire and metal bushing sample placed on a metallic holder frame used for the THz imaging experiment and the chart of the experimental setup.

the x axis was performed while the sample moved continuously at a velocity of 25 mm/s and the signal was read every 20 ms. After x axis scanning was finished, the sample was moved by 500 μm along the y axis and another scanning along the x axis was done again. In such a manner, the whole sample was raster scanned. The signal from the detector was read out using the conventional lock-in technique.

THz images of the sample were taken at distances from the OAP1 mirror (z) varying from 42 to 58 mm, whereas the focus distance of the OAP1 mirror employed in the experiment was 50 mm. The obtained image dataset contained 16 images of size 135 × 185 pixels that were transformed into an 8-bit format. Some of these images are shown in Fig. 2.

As it is seen, all of these images are quite blurry and contain visible noise which becomes more prominent as the distance from OAP1 increases. To suppress this noise, we have applied a modified discrete cosine transform filter with a hard spatial spectrum adapted threshold (also known as SSA DCT filter). The filtering procedure is described

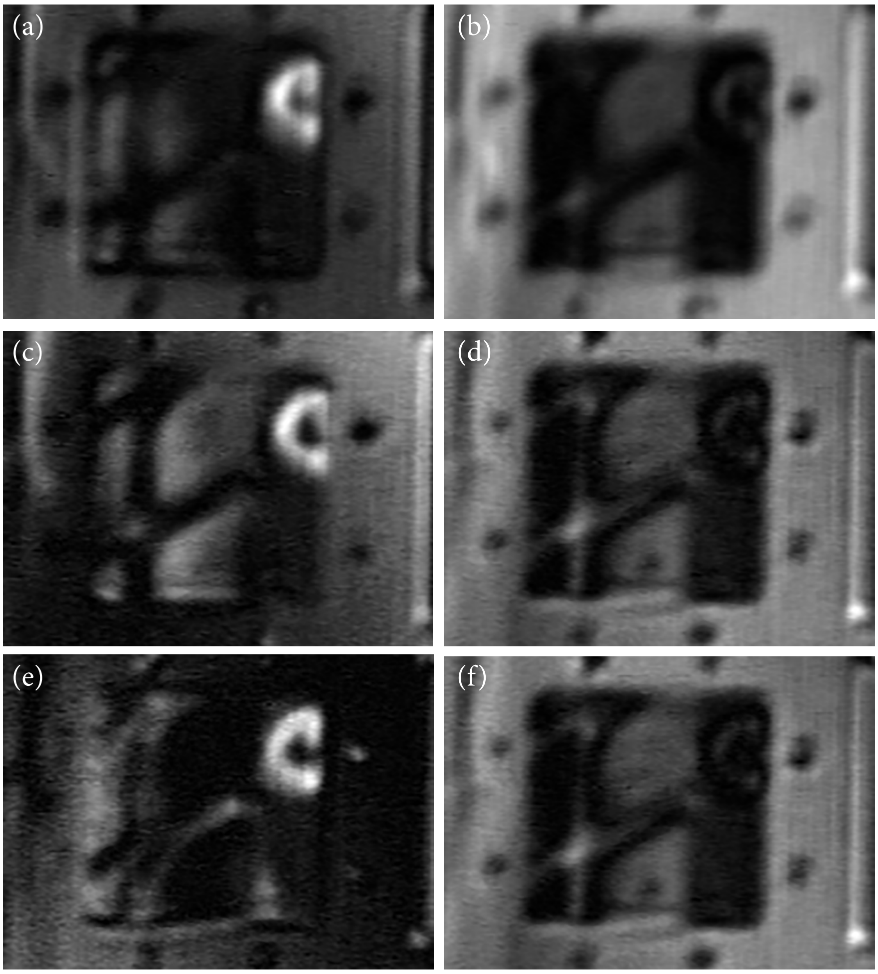

Fig. 2. Images of the sample obtained at different distances from the THz source along the z axis: 42 (a), 43 (b), 50 (c), 51 (d), 54 (e), 56 (f) mm.

in Ref. [8] and some of the images processed with the SSA DCT filter are shown in Fig. 3. Although the denoised images are visually more pleasant than the original ones, they are still very blurry, which complicates detection of some informational details. Thus, the purpose of our current research is to analyze the nature and behaviour of the blur mechanism in these images in order to select the best approach for its elimination.

Based on the imaging process, one can expect the presence of the defocus blur, which is supposed to be different for the images obtained at different distances from the OAP1 focus plane. Moreover, the sample moves while being scanned and, although the speed of its movement is low, due to the specifics of the recording equipment, it can become a reason for the motion blur. Finally, these images were subjected to SSA DCT filtering, which, along with noise removal, also affects the high-frequency image components. This is equivalent to some kind of low-pass filtering, and, therefore, can result in blur with the Gaussian-like behaviour. Thus, we expect that the THz images from our dataset will contain some combinations of the three types of blur described in Section 2. However, to determine the presence and contribution of each of the blur types, we need to examine these images using special methods.

4. Blur kernel investigation method and its performance for test data

To get more information on blur behaviour in the given THz images, we have chosen the kernel estimation method described in Ref. [41]. The method is based on the usage of phase-only image obtained in the Fourier domain and initially was designed for the detection of motion blur and estimating its length and angle. Indeed, the phase-only image has

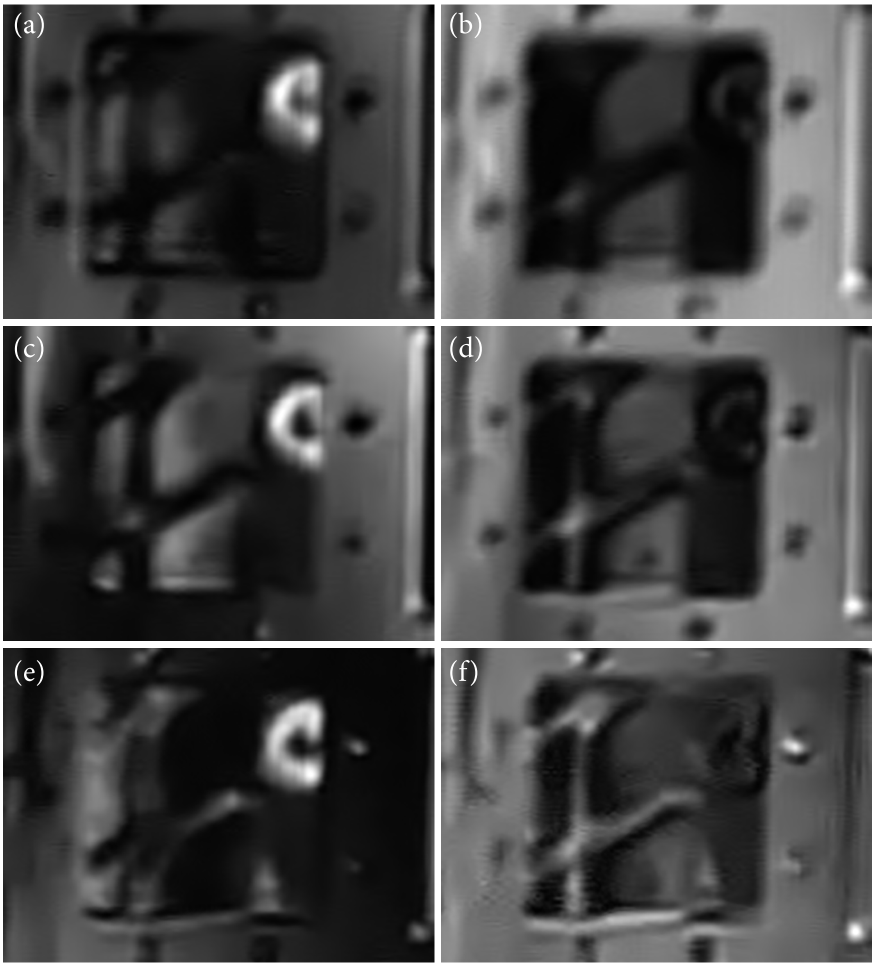

Fig. 3. Images of the sample obtained at different distances from the THz source along the z axis processed with the method given in Ref. [8]: 42 (a), 43 (b), 50 (c), 51 (d), 54 (e), 56 (f) mm.

a good potential in investigating the features of other types of blur as well.

In brief, the idea of using the phase-only image can be given as follows. In the Fourier domain, Eq. (2) corresponds to

$$F(I_b) = F(I_s) \odot F(k), \tag{7}$$

where $\odot$ represents the component-wise multiplication. The result of Fourier transform is a complex signal, for which phase and amplitude components can be calculated. If taking the phase of a complex signal is denoted by $P(\cdot)$, then

$$P(I_s) = F^{-1}(P(F(I_s))), \tag{8}$$

where F^{-1} is the inverse Fourier transform. Since Fourier components of an edge tend to be in phase with each other, the phase-only image works as some kind of an edge-extractor. The phase-only image of the convolution $P(I_s \otimes k)$ is equal to the convolution of the phase-only image and phase-only kernel,

$$P(I_s \otimes k) = F^{-1}(P(F(I_s \otimes k))) = P(I_s) \otimes P(k). \tag{9}$$

From Eq. (9) it follows that $P(I_b)$ is obtained by convolving $P(I_s)$ in the orientation of the linear kernel with the phase-only kernel. This results in the creation of multiple copies ('ghosts') of the phase-only image, $P(I_s)$, separated by the width of the kernel length, while the copies corresponding to the principal peaks will be the most noticeable.

The key advantage of the phase-only image is that it allows to simplify the effect of blurring by replacing the continuous smear in a blurred image by a simple sum of two (principal) copies in the phase-only blurred image. The existence of these multiple copies suggests using the autocorrelation of $P(I_b)$; however, since the phase-only image is completely self-uncorrelated, one should use the absolute value of phase-only image instead $(A(|P(I_b)|))$. Such autocorrelation function (ACF) is supposed to show the desired behaviour.

Now let us check how the phase-only image and the autocorrelation of its absolute value look for different types of blur and what information can be extracted from them.

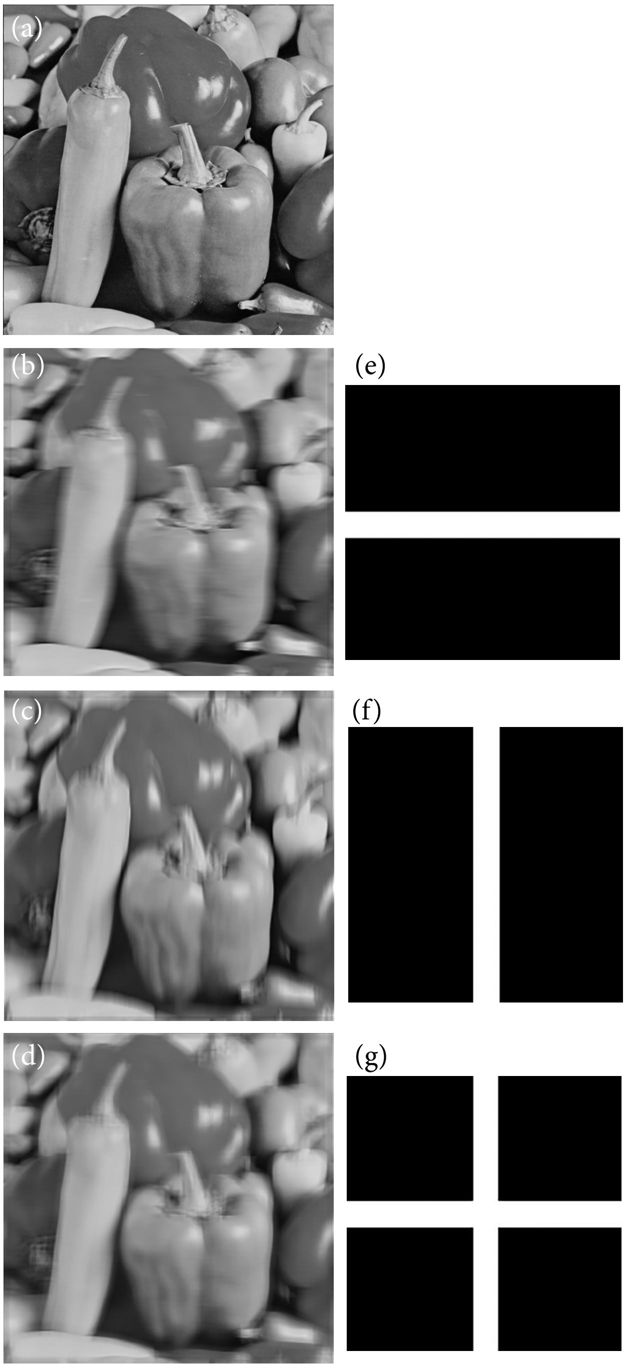

Fig. 4. Test image Peppers (a) and its versions blurred with the motion blur (b–d) with different blur kernels (e–g).

Figure 4(a) shows the test image Peppers and Fig. 4(b–d) show its versions blurred with the motion blur using the kernels depicted in Figs. 4(e) ('horizontal motion'), 4(f) ('vertical motion') and 4(g) ('horizontal and vertical motion'), respectively. The size of the matrix representing the blur kernel is 11 × 11 pixels. As seen in the 'horizontal motion' case, the image pixels are smeared in the horizontal direction, while for the 'vertical motion' the smearing is observed in the vertical direction. For the case of multidirectional motion, the picture is hazer, yet, if examined closely, one

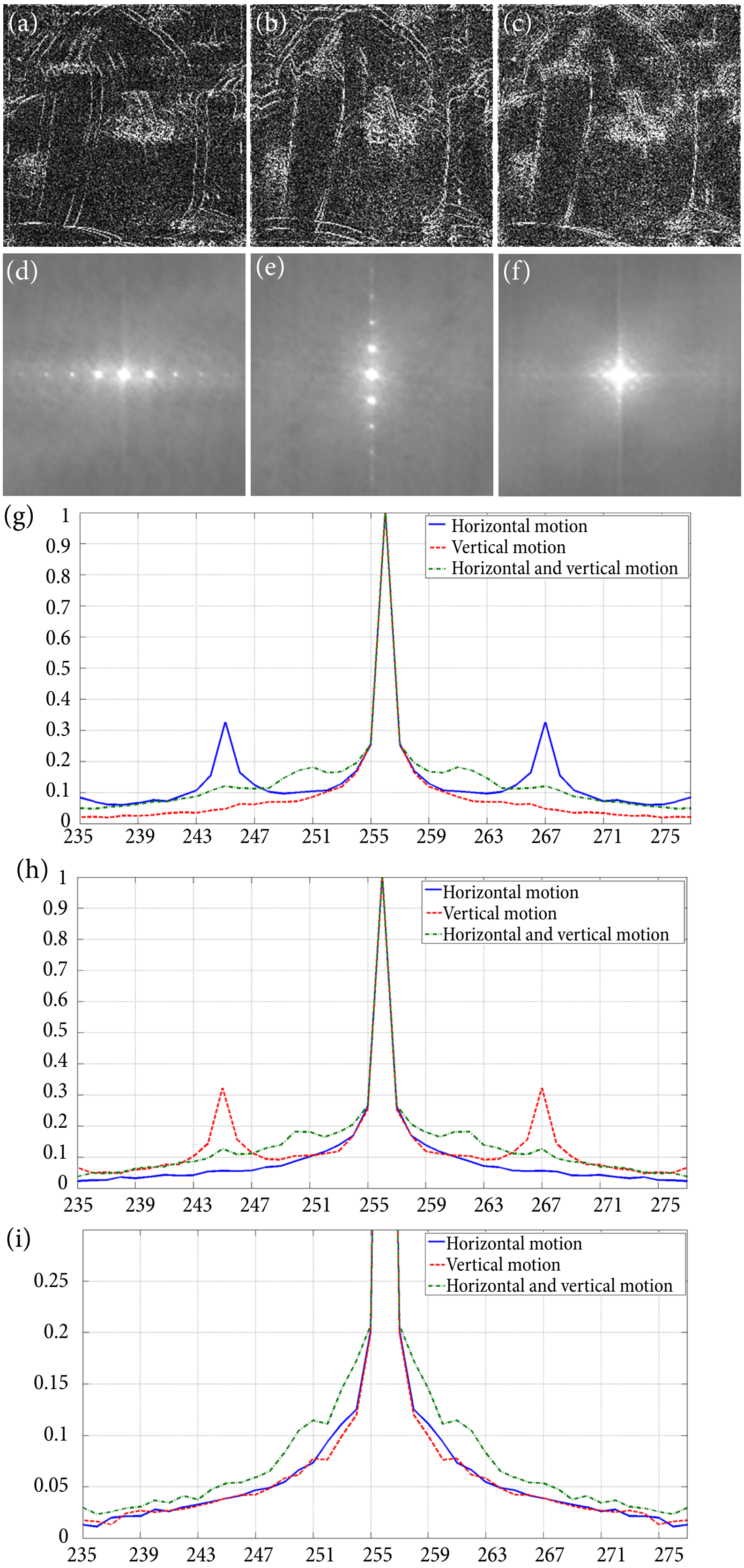

Fig. 5. Phase-only images of image Peppers (a–c), autocorrelations of phase-only images' absolute values (d–f) and their horizontal (g), vertical (h) and 45-degree central sections (i) for 'horizontal motion' (a, d), 'vertical motion' (b, e) and 'horizontal and vertical motion' (c, f), respectively.

can still notice the traces of pixels being smeared in the directions determined by the blur kernel, although this smearing is pronounced much less compared to the cases of unidirectional motion.

If motion is unidirectional, in phase-only Peppers images (Fig. 5(a, b)), one can clearly see the two copies of an image shifted in the direction determined by the blur kernel. In the graphs representing autocorrelation functions (Fig. 5(d, e)), this behaviour is reflected as bright points, repeating themselves in the blur direction with a certain period. To evaluate the shift distance, let us study the sections of autocorrelation functions given in Fig. 5(g, h), where the blue curve corresponds to the 'horizontal motion', the red curve to the 'vertical motion', and the green one to the 'horizontal and vertical motion'.

As can be seen, in the horizontal section, the blue curve contains clear maxima on both sides of the main lobe, while there are no extrema in the vertical section. The distance between the main peak and the first side peaks in the horizontal section is 11 pixels, which is equal to the true blur length. For the 'vertical motion', the situation is the same with the only difference that the needed features can be extracted from the vertical section. For both cases, no extrema can be found in the 45-degree section.

Considering the more complicated case of bidirectional motion it can be observed that the phase-only image (Fig. 5(c)) does not contain as clear shifted copies as in the cases of the horizontal only or vertical only motion. Nevertheless, the required information on the blur length still can be derived from the autocorrelation function (Fig. 5(f)) and its sections. As seen from Fig. 5(f), the repeating patterns spread in both directions from the centre, which may be considered as a pointer to the blur angle. In the sections, the side lobes are found in all the three views, although their amplitude is much lower than in unidirectional cases and the first side maxima appear at the distance that is twice less than the actual size of the blur kernel matrix. Yet, the second side lobe is shifted from the main peak by 11 pixels, which means that in the case of more complicated motion patterns the blur angle and length can be estimated from $A(|P(I_\mathrm{b})|)$.

Figure 6 shows the test image Peppers distorted with the defocus blur with different radiuses (11, 24 and 48 pixels) and the corresponding blur kernels (3). In this experiment, the size of the test image was 256 × 256 pixels.

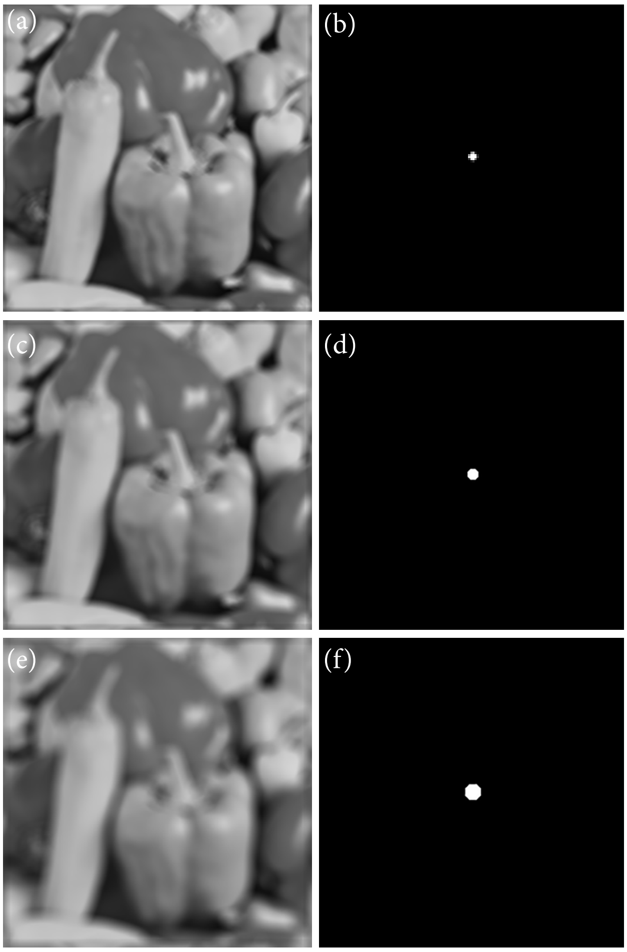

Fig. 6. Test image Peppers distorted with the defocus blur with different radiuses (a, c, e) and the corresponding blur kernels (b, d, f): 11 (a, b), 24 (c, d), 48 (e, f) pixels.

The first observation that can be made is that, unlike the motion blur, the defocus blur has no blurring direction but affects pixels in all directions equally. The larger the blur radius is, the less details can be seen in the blurred image.

Although the images containing the defocus blur look very different from the images affected by the motion blur, their phase-only images have a lot of similarities. Comparing the images from Fig. 5(a–c) and Fig. 7(a–c), it can be noticed that in both cases the shifted copies of an image are clearly seen, although the phase-only images for the defocus blur look noisier. The ACF for the defocus blur (Fig. 7(d–f)) looks quite specific. Its bright part forms a circle, while the larger defocus blur radius corresponds to the larger circle in the graph of ACF. However, as one can see from the sections (Fig. 7(g–i)), although there is a connection between the radius of circle in the graph of autocorrelation

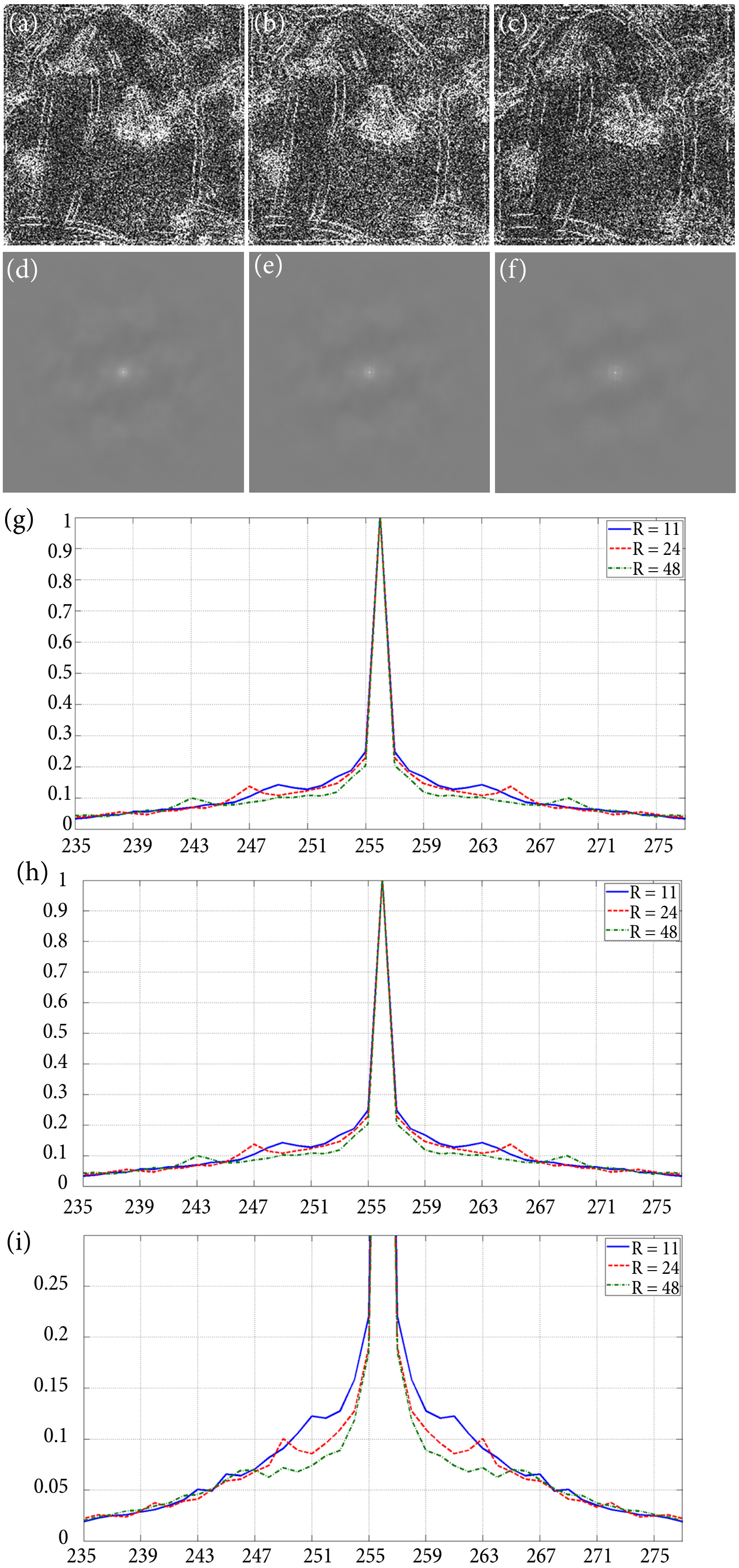

Fig. 7. Phase-only images (a–c), autocorrelations of phase-only images' absolute values (d–f) and their horizontal (g), vertical (h) and 45-degree central sections (i) for the defocus blur with different radiuses: 11 (a, d), 24 (b, e), 48 (c, f).

function and the defocus blur radius, the distance between the main peak and the side lobes does not seem to be proportional to the true radius of the defocus blur kernel. So, in general, it is possible to distinguish the defocus blur from the motion blur by the phase-only image and autocorrelation of its absolute value, yet in order to obtain numerical parameters describing this type of blur, one should additionally apply different tools for kernel estimation.

Figure 8(a, c, e) shows the test image Peppers distorted with the Gaussian blur with kernel 11 × 11 pixels modelled according to Eq. (5). Three cases have been considered: ‘Case 1’: $A = 1$, $a = 1.5$, $b = 0$, $c = -1.5$ (Fig. 8(b)); ‘Case 2’: $A = 1$, $a = 0.5$, $b = 0$, $c = -0.5$ (Fig. 8(d)); ‘Case 3’: $A = 1$, $a = 0.1$, $b = 0$, $c = -0.\ 1$ (Fig. 8(f)). As seen, for the considered shapes of the blur kernel, under some conditions images with the Gaussian blur may appear very similar to the ones with the defocus blur, as there is no smearing in a particular direction but the pixels are smoothed evenly. As for the phase-only images (Fig. 9(a–c)), depending on the parameters of the Gaussian function, they may look a bit similar to the phase-only images for the defocus blur as well, although the noise level can strongly vary. The autocorrelation functions (Fig. 9(d–f)), though, look very different from those for the defocus blur and look closer to the case of bidirectional motion. However,

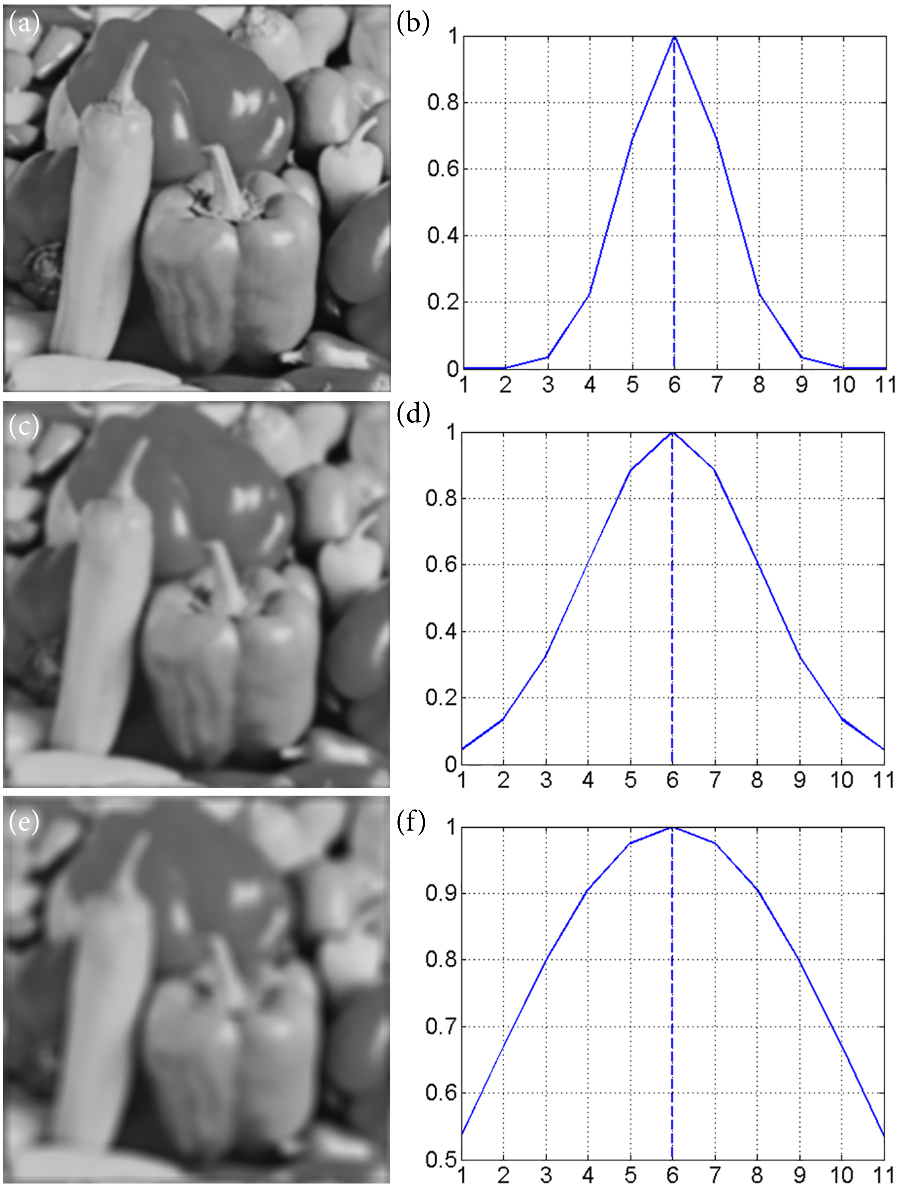

Fig. 8. Test image Peppers blurred with the Gaussian blur (a, c, e) with different blur kernels: ‘Case 1’ (a, b), ‘Case 2’ (c, d), ‘Case 3’ (e, f).

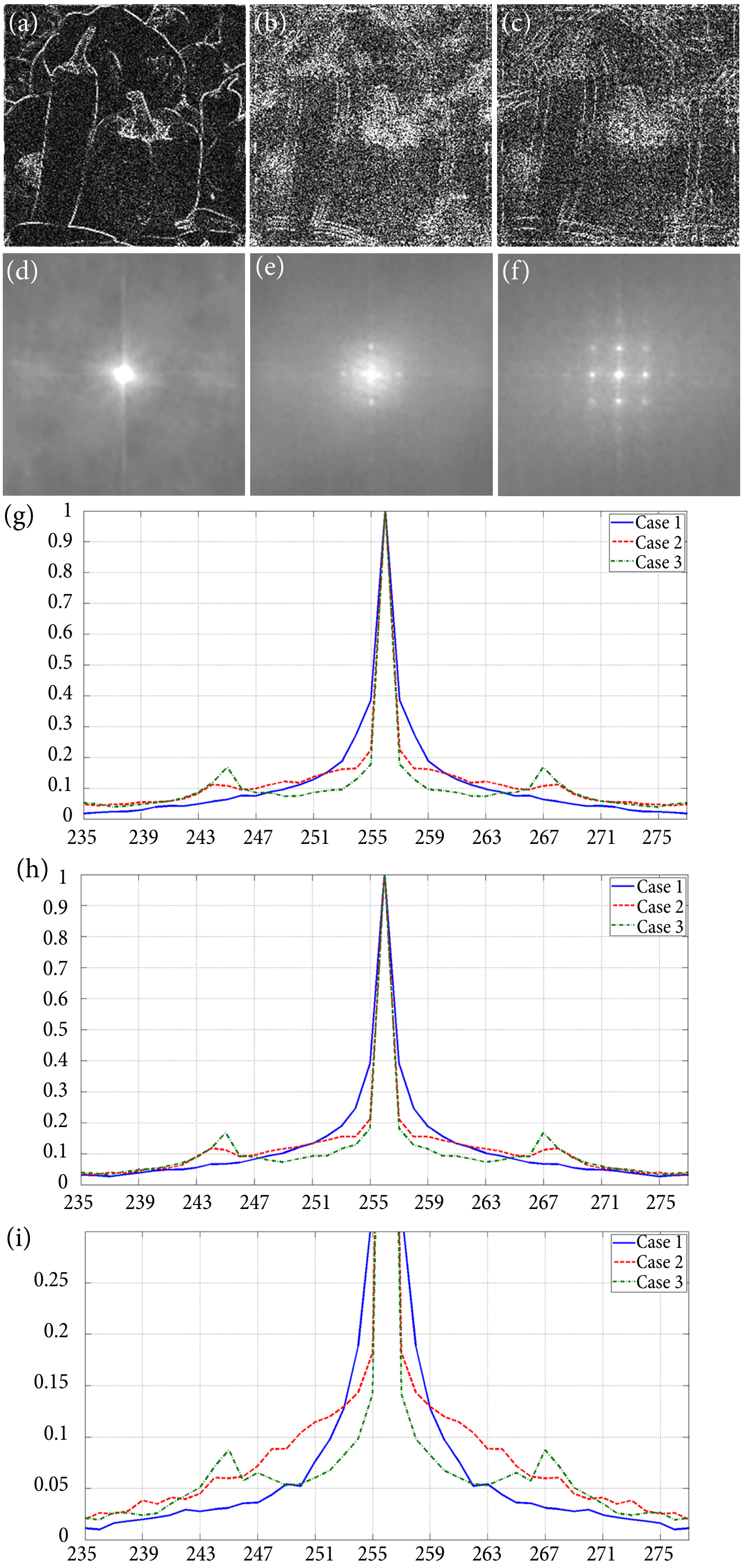

Fig. 9. Phase-only images (a–c), autocorrelations of phase-only images' absolute values (d–f) and their horizontal (g), vertical (h) and 45-degree central sections (i) for different cases of the Gaussian blur: 'Case 1' (a, d), 'Case 2' (b, e), 'Case 3' (c, f).

the exact features of autocorrelation functions depend on the parameters of the blur kernel strongly.

In ‘Case 1’, for example, the actual size of the blur kernel turns out to be much less than the true matrix size, so the image gets blurred only slightly. In the phase-only image, only one bold contour is present instead of the shifted copies of the image. The sections of autocorrelation function for this case contain no extrema and do not give any information on the blur length. The autocorrelation function for ‘Case 2’ shows much similarity to the case of bidirectional motion and contains a wide main lobe with weakly pronounced side lobes, which, nevertheless, are shifted from the main peak by a distance close to the true size of the blur kernel matrix. Finally, the autocorrelation function for ‘Case 3’ contains clearly expressed ‘ghosts’ spread in a grid from the main lobe where the shift determined as distance from the main peak to side lobes is equal to the true blur kernel.

Based on the results obtained for the test data, it can be concluded that, in general, by analyzing the phase-only image and the autocorrelation function of its absolute value one can detect features of different types of blur, although in some situations distinguishing between the Gaussian blur and the multidirectional motion blur can be problematic. For relatively simple cases of the motion blur, the use of the phase-only image allows one to determine the blur length and its angle, which can be used as an initial input for the iterative procedure of further kernel refinement. The same is valid for some cases of the Gaussian blur. Meanwhile, the defocus blur can be detected with the help of the phase-only image, but in order to obtain its radius one should apply additional tools.

Now, since the features of each type of blur are known, the phase-only images and autocorrelation functions of their absolute values for the THz images from the experimental dataset could be analyzed

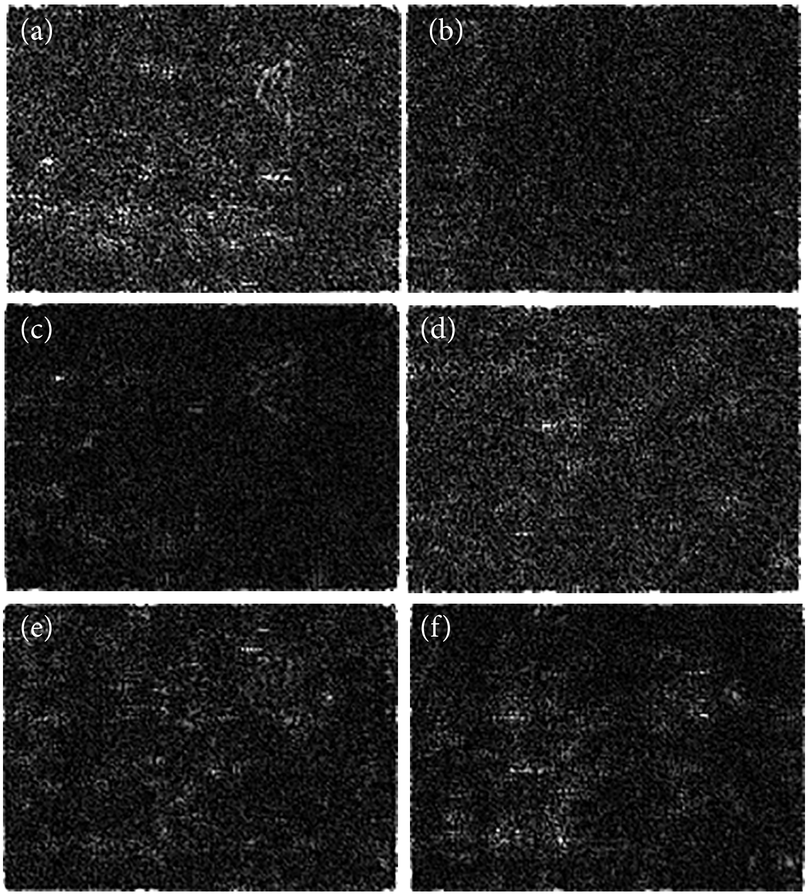

Fig. 10. Phase-only images calculated for the THz images obtained at different distances from the THz source along the z axis, processed with the method given in Ref. [8]: 42 (a), 43 (b), 50 (c), 51 (d), 54 (e), 56 (f) mm.

and conclusions on the nature and compound of blur there could be drawn.

5. Analysis of blur kernels of real THz images

Figure 10 shows the phase-only images obtained for the THz images presented in Fig. 3. The first observation that can be made from Fig. 10 is that none of the images contain clearly pronounced edges as it was for the test data. On the one hand, this may be because of the specific nature of blur in these images and, on the other hand, this may arise because of their low resolution. Another observation is that some images look noisier than the others and these are mostly the images taken at bigger distances from OAP1. The noisy appearance of the phase-only image supposedly indicates the increased level of the defocus and/or Gaussian blur.

In Fig. 11, one can find the autocorrelations calculated for the absolute values of phase-only images. Despite the expectations, these ACFs contain no clear signs of the defocus blur, but look more like the Gaussian blur (cases 1 and 2) or the bidirectional motion. There are two interesting features, though. Firstly, there are two clear bright stripes in horizontal and vertical directions, which did not manifest for the test data. This may be because of the difference in resolution, which is much lower for the THz images compared to the test image used. Secondly, the central parts of autocorrelation graphs become brighter and wider the further from the focus plane the object is. What is more, no regularly repeated extrema can be detected in autocorrelation plots.

To study the behaviour of ACFs, the horizontal and vertical sections presented in Fig. 12(a, c) and Fig. 12(b, d), respectively, are considered. For convenience, the plots for six images are given in the groups of three (42, 43, 50 mm for images 1–3 and 51, 54, 56 mm for images 4–6). As seen, the curves for images 1–3 have a peaky structure and a quite wide main lobe both in horizontal and vertical directions. This behaviour indicates the presence of some Gaussian-like component, while the peaky structure may be a sign of the motion blur. However, unlike the peaks for the motion blur in the test image, the local maxima in real images are located more densely than it would be expected to consider them as 'ghosts', so some of them obviously indicate the features that have not been studied on the test examples. At the same time, for images 2 and 3, there are clearly pronounced peaks similar to the ones that were observed for the motion blur patterns in the test image. Moreover, there are peaks that appear almost simultaneously for different images, which, possibly, could be used in determining the blur length.

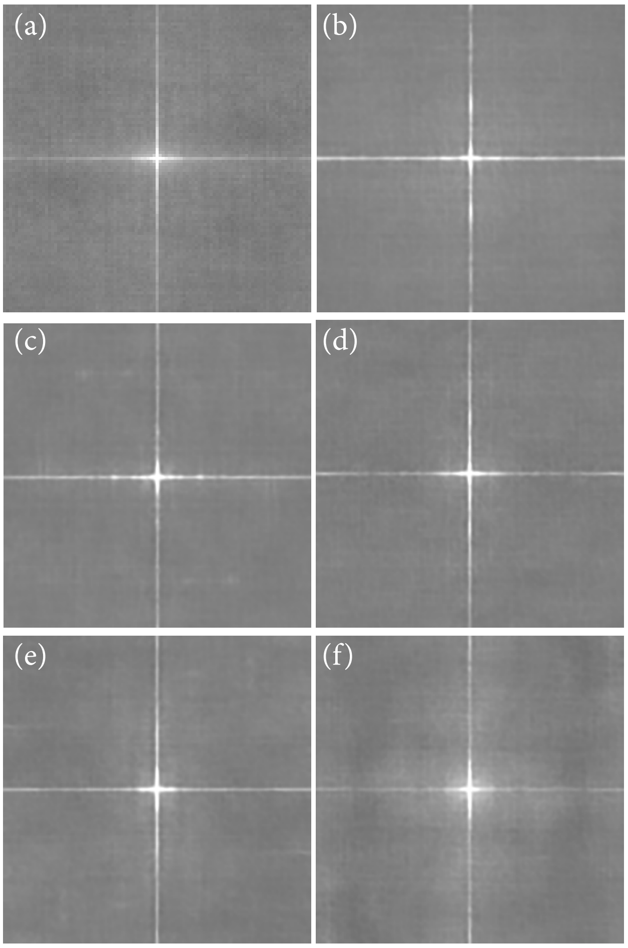

Fig. 11. Autocorrelation functions for the absolute values of the phase-only images calculated for the THz images obtained at different distances from the THz source along the z axis, processed with the method given in Ref. [8]: 42 (a), 43 (b), 50 (c), 51 (d), 54 (e), 56 (f) mm.

For images 4–6, the side lobes are generally lower than for images 1–3, while the main lobe is wider. The peaky structure is less pronounced, which may indicate the prevailing of a Gaussian-like component over the motion-caused blur. Again, there are intervals where some kinds of local peaks can be observed for all the images and such points seem to be most promising in terms of determining the blur length.

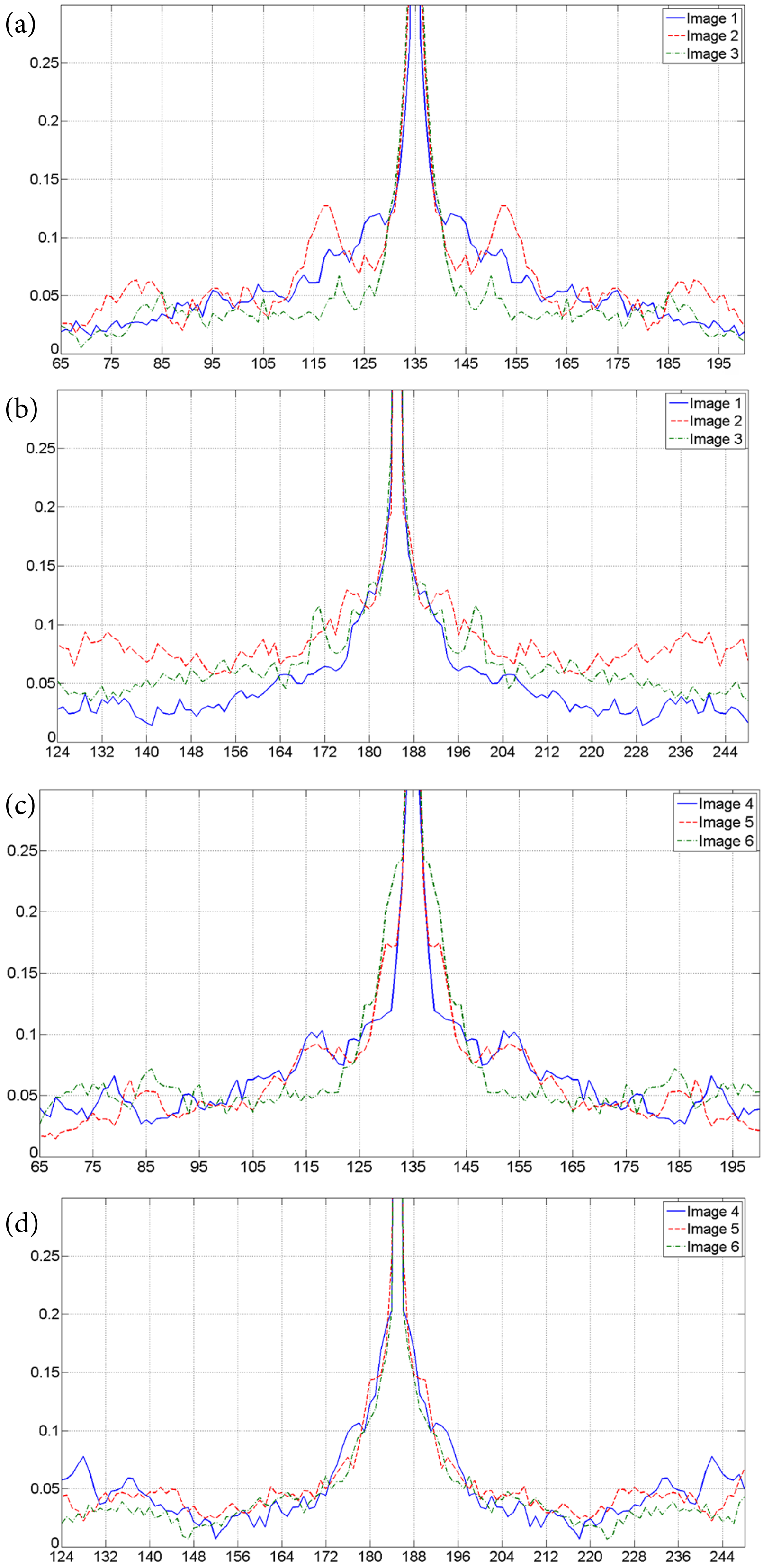

Fig. 12. Horizontal (a, c) and vertical (b, d) sections of the autocorrelation functions for the absolute values of the phase-only images calculated for the THz images obtained at different distances from the THz source: 42 mm (image 1), 43 mm (image 2), 50 mm (image 3), 51 mm (image 4), 54 mm (image 5), 56 mm (image 6).

In general, the behaviour of the phase-only image and the autocorrelation of its absolute value is quite complicated and indicates the presence of several components of blur. The contribution of these components differs depending on the distance from OAP1 the images were taken at.

6. Conclusions

Despite the significant advances in the field of terahertz imaging over the last decades, there are still a number of problems that lead to the poor quality of the resulting images, in particular, their essential blurring accompanied with noise. Since most of these problems are difficult to solve at a hardware level, attempts to overcome them through the use of digital image processing methods have been made.

The paper addresses the problem of THz images deblurring, namely, the stage of evaluating the blur kernel in order to use the obtained information while designing a corresponding image enhancement method. To investigate the parameters of blur kernels the phase-only image method has been used.

The phase-only images and ACFs of their absolute values have been calculated for the most widespread types of blur. As a result of the analysis on the test data, the characteristic features allowing one to distinguish between different types of blur have been formulated.

Aiming to investigate the nature and behaviour of blur in real-life THz images, the phase-only image approach has been applied to a set of images obtained using a basic imaging setup operating at a frequency of 0.1 THz. It has been shown that the blur in these images is of mixed nature, containing Gaussian-like and motion blur components, while the contribution of each of them differs depending on the distance from a parabolic mirror the images were taken at. Although the phase-only image approach gives some valuable information on the nature of blur mechanisms in the images under study, to obtain a blur kernel model suitable for further usage within a deblurring pipeline, it is needed to study the parameters of blur in more detail using additional tools. This will be the task for further research on this topic.

Acknowledgements

This research was funded by a Grant (No. P-LU-PAR-23-26) from the Research Council of Lithuania and supported by Marius Jakulis Jason Foundation within the Special Program 'For Ukraine's Science'.

References

[1] Y. Takida, K. Nawata, and H. Minamide, Security screening system based on terahertz-wave spectroscopic gas detection, Opt. Express **29**(2), 2529–2537 (2021).

[2] J.F. Federici, B. Schulkin, F. Huang, D. Gary, R. Barat, F. Oliveira, and D. Zimdars, THz imaging and sensing for security applications – explosives, weapons and drugs, Semicond. Sci. Technol. **20**(7), 266–280 (2005).

[3] N. Palka, M. Szustakowski, M. Kovalski, T. Trzcinski, R. Ryniec, M. Piszczek, W. Ciurapinski, M. Zyczkowski, P. Zagrajek, and J. Wrobel, THz spectroscopy and imaging in security applications, in: *Proceedings of the 19th International Conference on Microwaves, Radar & Wireless Communications* (2012) pp. 265–270.

[4] M. Lu, J. Shen, N. Li, Y. Zhang, C. Zhang, L. Liang, and X. Xu, Detection and identification of illicit drugs using terahertz imaging, J. Appl. Phys. **100**, 103104 (2006).

[5] P. Bawuah, D. Markl, D. Farrell, M. Evans, A. Portieri, A. Anderson, D. Goodwin, R. Lukas, and J.A. Zeitler, Terahertz-based porosity measurement of pharmaceutical tablets: a tutorial, J. Infrared Millim. Terahertz Waves **41**, 450–469 (2020).

[6] I. Kašalynas, R. Venckevičius, L. Minkevičius, A. Sešek, F. Wahaia, V. Tamošiunas, B. Voisiat, D. Seliuta, G. Valušis, A. Švigelj, and J. Trontelj, Spectroscopic terahertz imaging at room temperature employing microbolometer terahertz sensors and its application to the study of carcinoma tissues, Sensors **16**(4), 432 (2016).

[7] Y. Liu, H. Liu, M. Tang, J. Huang, W. Liu, J. Dong, X. Chen, W. Fu, and Y. Zhang, The medical application of terahertz technology in non-invasive

detection of cells and tissues: opportunities and challenges, RSC Adv. **9**, 9354–9363 (2019).

[8] M. Karaliūnas, K.E. Nasser, A. Urbanowicz, I. Kašalynas, D. Bražinskenė, S. Asadauskas, and G. Valušis, Non-destructive inspection of food and technical oils by terahertz spectroscopy, Sci. Rep. **8**, 18025 (2018).

[9] L. Afsah-Hejri, P. Hajeb, P. Ara, and R.J. Ehsani, A comprehensive review on food applications of terahertz spectroscopy and imaging, Compr. Rev. Food Sci. Food Saf. **18**(5), 1563–1621 (2019).

[10] K. Krügener, J. Ornik, L.M. Schneider, A. Jackel, C.L. Koch-Dandolo, E. Castro-Camus, N. Riedl-Siedow, M. Koch, and W. Viol, Terahertz inspection of buildings and architectural art, Appl. Sci. **10**(15), 5166 (2020).

[11] G. Valušis, A. Lisauskas, H. Yuan, W. Knap, and H.G. Roskos, Roadmap of Terahertz Imaging 2021, Sensors **21**(12), 4092 (2021).

[12] D. Jokubauskis, L. Minkevičius, D. Seliuta, I. Kašalynas, and G. Valušis, Terahertz homodyne spectroscopic imaging of concealed low-absorbing objects, Opt. Eng. **58**(2), 023104 (2019).

[13] L. Minkevičius, V. Tamošiūnas, I. Kašalynas, D. Seliuta, G. Valušis, A. Lisauskas, S. Boppel, H.G. Roskos, and K. Kohler, Terahertz heterodyne imaging with InGaAs-based bow-tie diodes, Appl. Phys. Lett. **99**, 131101 (2011).

[14] B.K. Kundu and Pragti, THz image processing and its applications, in: *Generation, Detection and Processing of Terahertz Signals. Lecture Notes in Electrical Engineering*, Vol. 794 (Springer, Singapore, 2022) pp. 123–137.

[15] Y. Li, W. Hu, X. Zhang, Z. Xu, J. Ni, and L.P. Ligthart, Adaptive terahertz image super-resolution with adjustable convolutional neural network, Opt. Express **28**(15), 22200–22217 (2020).

[16] Z. Long, T. Wang, Ch. You, Z. Yang, K. Wang, and J. Liu, Terahertz image super-resolution based on a deep convolutional neural network, Appl. Opt. **58**(10), 2731–2735 (2019).

[17] Z. Chen, C. Wang, J. Feng, Z. Zou, F. Jiang, H. Liu, and Y. Jie, Identification of blurred terahertz images by improved cross-layer convolutional neural network, Opt. Express **31**(10), 16035–16053 (2023).

[18] V. Abramova, S. Abramov, V. Lukin, I. Grigelionis, L. Minkevičius, and G. Valušis, Improvement of terahertz images by adaptive discrete cosine transform (DCT)-based denoising, Lith. J. Phys. **62**(4), 267–276 (2022).

[19] S. Abramov, M. Uss, V. Abramova, V. Lukin, B. Vozel, and K. Chehdi, On noise properties in hyperspectral images, in: *IGARSS'2015* (2015) pp. 3501–3504.

[20] O. Rubel, V. Lukin, S. Krivenko, V. Pavlikov, S. Zhyla, and E. Tserne, Reduction of spatially correlated speckle in textured SAR images, Int. J. Comp. **20**(3), 319–327 (2021).

[21] V. Abramova, S. Krivenko, V. Lukin, and O. Krylova, Analysis of noise properties in dental images, in: *ELNANO 2020*, Vol. 9088768 (Milan, Italy, 2020) pp. 511–515.

[22] V. Abramova, S. Abramov, and V. Lukin, Iterative method for blind evaluation of mixed noise characteristics on images, Inform. Telecommun. Sci. **6**(1), 8–14 (2015).

[23] K. Zhang, W. Ren, W. Luo, W.-S. Lai, B. Stenger, M.-H. Yang, and H. Li, Deep image deblurring: a survey, Int. J. Comput. Vis. **130**, 2103–2130 (2022).

[24] Y. Lu, Out-of-focus blur: Image de-blurring, arXiv preprint, arXiv:1710.00620 (2017).

[25] X. Zhang, Gaussian distribution, in: *Encyclopedia of Machine Learning*, eds. C. Sammut, G.I. Webb (Springer, Boston, MA, 2011) pp. 425–428.

[26] E. Kalalembang, K. Usman, and I.P. Gunawan, DCT-based local motion blur detection, in: *Proceedings of the International Conference on Instrumentation, Communication, Information Technology, and Biomedical Engineering* (Bandung, Indonesia, 2009) pp. 1–6.

[27] F. Yang, Y. Huang, Y. Luo, L. Li, and H. Li, Robust image restoration for motion blur of image sensors, Sensors **16**(6), 845 (2016).

[28] C. Seibold, A. Hilsmann, and P. Eisert, Model-based motion blur estimation for the improvement of motion tracking, Comput. Vis. Image Underst. **160**, 45–56 (2017).

[29] C. Mei and I. Reid, Modeling and generating complex motion blur for real-time tracking, in: *Proceedings of the IEEE Conference on Computer*

Vision and Pattern Recognition (Anchorage, AK, USA, 2008) pp. 1–8.

[30] T. Brooks and J.T. Barron, Learning to synthesize motion blur, in: *Proceedings of the 2019 IEEE/CVF Conference on Computer Vision and Pattern Recognition (CVPR)* (Long Beach, CA, USA, 2019) pp. 6833–6841.

[31] R.A. Haddad and A.N. Akansu, A class of fast Gaussian binomial filters for speech and image processing, IEEE Trans. Signal Process. **39**, 723–727 (1991).

[32] D. Krishnan and R. Fergus, Fast image deconvolution using hyper-Laplacian priors, in: *Advances in Neural Information Processing Systems* (NIPS, 2009) pp. 1033–1041.

[33] D. Zoran and Y. Weiss, From learning models of natural image patches to whole image restoration, in: *Proceedings of the International Conference on Computer Vision* (Barcelona, Spain, 2011) pp. 479–486.

[34] W. Ren, J. Pan, X. Cao, and M.-H. Yang, Video deblurring via semantic segmentation and pixel-wise non-linear kernel, in: *Proceedings of the IEEE International Conference on Computer Vision (ICCV)* (Venice, Italy, 2017) pp. 1086–1094.

[35] J. Kruse, C. Rother, and U. Schmidt, Learning to push the limits of efficient FFT-based image deconvolution, in: *Proceedings of the IEEE International Conference on Computer Vision (ICCV)* (Venice, Italy, 2017) pp. 4596–4604.

[36] A. Foi, K. Dabov, V. Katkovnik, and K. Egiazarian, Shape-adaptive DCT for denoising and image reconstruction, Proc. SPIE **6064**, A-18 (2006).

[37] S. Cho, J. Wang, and S. Lee, Handling outliers in non-blind image deconvolution, in: *Proceedings of the 2011 International Conference on Computer Vision* (Barcelona, Spain, 2011) pp. 495–502.

[38] Y. Nan, Y. Quan, and H. Ji, Variational-EM-based deep learning for noise-blind image deblurring, in: *Proceedings of the IEEE/CVF Conference on Computer Vision and Pattern Recognition (CVPR)* (Seattle, WA, USA, 2020) pp. 3623–3632.

[39] L. Pan, Y. Dai, and M. Liu, Single image deblurring and camera motion estimation with depth map, in: *Proceedings of the IEEE Winter Conference on Applications of Computer Vision (WACV)* (Waikoloa Village, HI, USA, 2019) pp. 2116–2125.

[40] M. McKenney and M. Schneider, *Map Framework: A Formal Model of Maps as* a *Fundamental Data Type in Information Systems* (Springer Cham, 2016).

[41] L. Pan, R. Hartley, M. Liu, and Y. Dai, Phase-only image based kernel estimation for single image blind deblurring, in: *Proceedings of the IEEE/CVF Conference on Computer Vision and Pattern Recognition (CVPR)* (Long Beach, CA, USA, 2019) pp. 6027–6036.

[42] L. Li, J. Pan, W.-S. Lai, C. Gao, N. Sang, and M.-H. Yang, Learning a discriminative prior for blind image deblurring, in: *Proceedings of the IEEE Conference on Computer Vision and Pattern Recognition* (2018) pp. 6616–6625.

[43] X. Tao, H. Gao, X. Shen, J. Wang, and J. Jia, Scale-recurrent network for deep image deblurring, in: *Proceedings of the IEEE/CVF Conference on Computer Vision and Pattern Recognition* (Salt Lake City, UT, USA, 2018) pp. 8174–8182.

KAUKIŲ, LEMIANČIŲ TERAHERCINIŲ VAIZDŲ SULIEJIMĄ, TYRIMAS

V. Abramova [a, b], S. Abramov [a], V. Lukin [a], I. Grigelionis [b], L. Minkevičius [b], G. Valušis [b]

[a] *Nacionalinio aerokosmoso universiteto Informacijos ir komunikacijos technologijų departamentas, Charkivas, Ukraina*
[b] *Fizinių ir technologijos mokslų centro Optoelektronikos skyrius, Vilnius, Lietuva*

Santrauka

Šiame darbe aptariamos skaitmeninio terahercinių vaizdų apdorojimo problemos. Nepaisant vis tobulinamos aparatūrinės terahercinių vaizdų užrašymo dalies, jų kokybė vis tiek nukenčia dėl žemos skyros ar vaizdo suliejimo. Norint padidinti vaizdų kokybę galima naudoti tam tikrus skaitmeninius duomenų apdorojimo metodus. Didelis dėmesys skiriamas triukšmo filtravimo metodų vystymui, tačiau norint apčiuopiamai pagerinti vaizdų kokybę nemažiau svarbūs yra gerokai mažiau tyrinėti suliejimo mažinimo metodai. Todėl šiame darbe tiriamos ir analizuojamos suliejimo funkcijų savybės bei konstruojamas suliejimo pašalinimo iš terahercinių vaizdų mechanizmas. Tam šiuo atveju yra naudojami faziniai vaizdai. Trijų dažniausiai pasitaikančių (išfokusavimo, judėjimo, Gauso) suliejimo mechanizmų tyrimai su testinėmis matomos šviesos nuotraukomis atskleidė galimybę nustatyti suliejimo mechanizmų prigimtį bei jų parametrus. Tačiau eksperimente užrašytų terahercinių vaizdų atveju pastebėta, kad suliejimo mechanizmai yra visiškai kiti nei testiniuose vaizduose, o norint pagrįsti sudėtingą jų prigimtį reikalingi papildomi tyrimai.